International Journal of Mass Spectrometry 345–347 (2013) 153–159

Contents lists available at SciVerse ScienceDirect

International Journal of Mass Spectrometry

journal homepage: www.elsevier.com/locate/ijms

Charge detection mass spectrometry for single ions with a limit of detection of 30 charges

Nathan C. Contino, Martin F. Jarrold*

Chemistry Department, Indiana University, 800 E. Kirkwood Avenue, Bloomington, IN 47405, United States

ARTICLE INFO

Article history:
Received 2 May 2012
Received in revised form 2 July 2012
Accepted 10 July 2012
Available online 20 July 2012

Keywords:
Charge detection mass spectrometry
Instrumentation

ABSTRACT

A charge detection mass spectrometer (CDMS) with a limit of detection of 30 elementary charges (e) for a single ion is described. The new CDMS consists of an electrospray source coupled to a dual hemispherical deflection analyzer (HDA) followed by a modified cone trap incorporating an image charge detector. Ions are energy selected by the dual HDA prior to entering the trap. The fundamental oscillation frequency of the trapped ion is extracted by a fast Fourier transform (FFT). The oscillation frequency and kinetic energy provide the m/z. The magnitude of the FFT at the fundamental frequency is proportional to the charge. Simulations indicate that the charge is measured with an average uncertainty of 3.2 e. The mass of each ion is obtained from the m/z and the charge. Mass distributions have been measured for bovine serum albumin (BSA). The BSA ions were trapped for up to 1139 cycles. BSA monomer and multimer ions are evident in the measured mass distribution. The width of the monomer mass distribution (14 kDa) is consistent with the predicted uncertainty in the charge.

1. Introduction

Charge detection mass spectrometry has garnered interest in the last two decades as a method for deconvoluting the complex mass spectra of macroions. Large ions, like protein complexes, can access a large number of charge states and frequently show a distribution of masses due to inherent heterogeneity, incomplete dehydration, or residual salt ions. These factors often lead to a spectrum consisting of a broad envelope of unresolved charge states spanning a wide range of m/z values, because most mass analyzers lack the resolution necessary to separate the closely spaced peaks. If the charge states cannot be resolved, the charge cannot be established, and the mass of the ion cannot be determined.

Charge detection mass spectrometry circumvents these problems by directly measuring the charge on an individual ion. As a charged particle passes through a metal cylinder, an image charge of equal magnitude is induced on the cylinder. Concurrent velocity measurements for ions with a known kinetic energy yield the m/z values, enabling the mass of each ion to be calculated. Early work focused on the charging and sizing of micron-sized particles for micro-meteroid experiments [1,2] and studying charged oil droplets [3].

Benner and Fuerstenau and their collaborators [4–8] were the first to combine an image charge detector tube with an electrospray source to investigate charge detection capabilities with macromolecules. Subsequently, Benner used an ion trap with a charge detector in the center to improve the precision of the charge measurement. The trap allows for multiple charge measurements with a single ion. If n equals the number of measurements averaged, the noise is decreased by a factor of $n^{1/2}$ [6]. Benner's noise level was 50 elementary charges (e) RMS after passing through a semi-Gaussian filter, which should decrease to 2.3 e RMS with the maximum number of oscillations reported (450). However, measurements were limited to charges larger than 250 electrons. In subsequent work, whole viruses were analyzed [7,8], although inaccurate charge measurements led to a significant error (±15%) in the mass determination.

Another approach to obtaining multiple charge measurements for a single ion is a linear array of charge detectors. Gamero-Castaño [9,10] has described a system of two interdigitated channels with three detector tubes in each. The overall noise level was ~100 e. A differential retarding potential energy analyzer was used to preselect the energy of the ions transmitted through the detector array. Recently our group has reported studies with a linear array of 22 detectors separated into two channels which are operated at different voltages [11]. Using this approach the energy and velocity of each ion can be measured in the detector array, so it is not necessary to preselect the energy. Poly(ethylene oxide) ions (300 kDa) with as few as 100 charges were detected using this design with an uncertainty of around 10 e.

Previous CDMS work in our group has focused on investigating the properties of charged water droplets generated by electrospray and their aerodynamic break-up in a capillary interface [12–14]. Antoine and Dugourd and their collaborators [15] have used CDMS

* Corresponding author.
E-mail address: mfj@indiana.edu (M.F. Jarrold).

1387-3806/$ – see front matter © 2012 Elsevier B.V. All rights reserved.
http://dx.doi.org/10.1016/j.ijms.2012.07.010

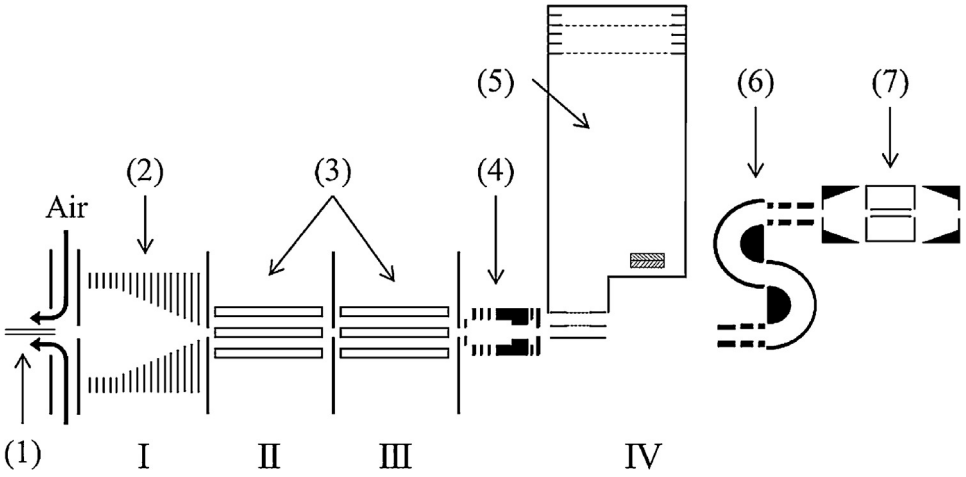

Fig. 1. Overview of the experimental apparatus. I, II, III, and IV show the four differentially pumped regions of the apparatus. (1) Electrospray emitter; (2) ion funnel; (3) hexapoles; (4) focusing lens; (5) orthogonal TOF-MS; (6) HDA; (7) modified cone trap with image charge detector.

to probe the maximum charge that can be held by different sizes of large poly(ethylene oxide) molecules (1–7 MDa). They have also used a CDMS trap for photodissociation studies of large molecules [16].

In work related to that described here, Zajfman and collaborators have reported several studies using an electrostatic ion trap with a charge detector to trap packets of ions [17]. They demonstrated that under some conditions the ion packet undergoes phase synchronization (i.e., the packets do not spread-out with time) [18,19]. Mass spectra were obtained from Fourier transform of the signal from the oscillating ion packets [20,21].

In the work reported in this paper our objective is to improve the accuracy and limits of detection of charge detection mass spectrometry for single macroions. In the new instrument described here we interface an ion trap, based on the "cone trap" design of Schmidt et al. [22], with a high resolution energy analyzer. A fast Fourier transform (FFT) is used to extract the oscillation frequency of the trapped ions. The magnitude of the FFT is proportional to the charge on the macroion (as well as to the trapping time).

The oscillation frequency is related to the m/z of the ion, but also depends on the ion's kinetic energy. To reduce the uncertainty in the m/z determination, a dual hemispherical deflection analyzer (HDA) was employed to select a narrow window of ion kinetic energies to introduce into the trap. The HDA consists of two concentric hemispherical electrodes, held at different potentials, which produce an electric field proportional to $1/r^2$. The electrode potentials determine which kinetic energies are passed. Carefully choosing these potentials, as well the location and diameter of the entrance and exit apertures, improves the energy resolution of the HDA [23,24]. Once the charge, oscillation frequency, and kinetic energy are known, it is a trivial matter to calculate the m/z and mass of each ion.

The performance of the new instrument is investigated by measuring mass distributions for bovine serum albumin (BSA) ions and BSA multimer ions. BSA is relatively small (66.4 kDa). It was selected as a test case because larger ions, the usual target for CDMS, often show a distribution of masses due to residual solvent and counter ions. This distribution makes it difficult to evaluate the performance (mass resolving power) of the new CDMS instrument.

2. Overview of the experimental apparatus

A schematic diagram of the experimental apparatus is shown in Fig. 1. Ions are created via electrospray ionization (ESI) using zero dead-volume nanospray fittings connected to a polyimide coated fused silica capillary (Polymicro) with an initial 75 μm inner diameter (ID), heated and pulled to yield a smaller ID. The emitter tip was coupled to a syringe pump (Cole-Parmer, EW-74900-00) which provided a constant flow rate of 30 μL/h. The ESI tip was held at a potential of 2–4 kV. Ions enter the vacuum chamber through a 0.5 mm diameter stainless steel aperture. A counter flow of hot, dry air helps to desolvate the ions. Bovine serum albumin (Sigma–Aldrich) was prepared at a concentration of 2 mg/mL in a 90:10 (v/v) water–acetonitrile mixture with 2% (v/v) acetic acid added.

The instrument is divided into four differentially pumped regions (see Fig. 1). The first region contains an ion funnel [25] composed of 96 plates spaced 1.25 mm apart, with a final aperture diameter of 2.54 mm. A 5.4 V/cm potential gradient is applied along the length of the ion funnel. A 600 kHz 40 V peak to peak RF potential, obtained from a home-built RF generator, is applied to the ion funnel to provide the pseudopotential that focuses the ions.

Two sets of hexapoles guide the ions through the next two differentially pumped regions. The 100 V DC potential applied to the first hexapole determines the nominal ion kinetic energy. The entry to the fourth and final differentially pumped region is marked by the presence of a focusing lens system. Several groups have published results showing improved ion beam focusing with minimal aberrations using an asymmetric einzel lens [26–28]. The design here, consisting of seven copper lenses with polyether ether ketone (PEEK) used for spacing and alignment, is modeled after that of Saito et al. [27].

Within the main chamber there are two possible paths available. Ions can either be analyzed by an orthogonal reflectron [29] time-of-flight mass spectrometer (TOF-MS) or continue on toward the dual hemispherical deflection analyzer and ion trap. To measure a TOF mass spectrum the potentials on the focusing lens are chosen such that the ion beam is focused at the extraction region of the TOF-MS. The extraction region consists of three plates, a central grounded plate and two pulsed plates which extract a group of ions and accelerate them vertically into the field free region of the TOF. The reflectron causes the ions to follow a parabolic path where they are detected by a pair of microchannel plates in a chevron configuration. The TOF is used as a diagnostic of the electrospray source.

If the TOF extraction plates are grounded, the ion beam passes into the entrance of the dual hemispherical deflection analyzer (HDA). As shown in Fig. 2, the two HDAs are placed in an S-shaped tandem arrangement, allowing the ion beam to maintain its original direction. Each HDA consists of two concentric hemispheres

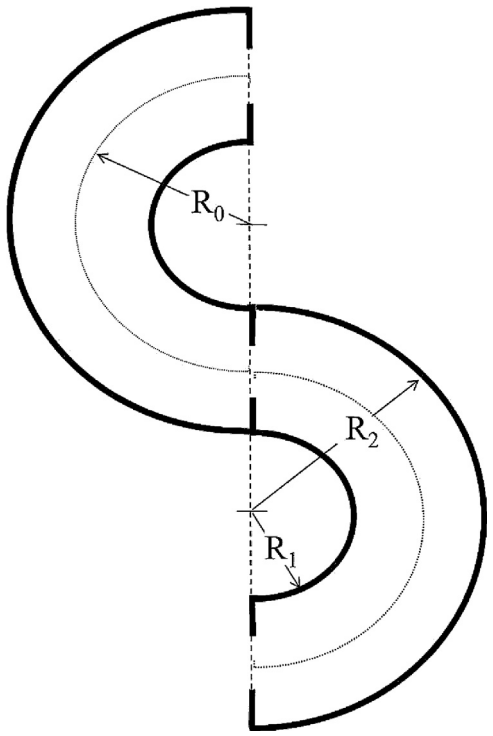

Fig. 2. Diagram of the dual HDA, showing the radii of the inner hemisphere, R_1, outer hemisphere, R_2, and central radius, R_0.

with radii R_1 = 19.05 mm and R_2 = 31.75 mm for the inner and outer hemispheres, respectively. The central radius is defined by:

$$R_0 = \frac{R_1 + R_2}{2} \tag{1}$$

and the potentials on the inner (V_1) and outer (V_2) hemispheres are given by [30]:

$$V_i = 2V_0 \left(\frac{R_0}{R_i} - 1 \right) \tag{2}$$

with i = 1 and 2. V_0 in Eq. (2) is the potential at radius R_0 and it is also the kinetic energy of the ions to be selected.

The cone trap [22] consists of two conical end caps located 95.25 mm apart with a 6.35 mm diameter aperture. A charge detector tube (25.4 mm long, 6.35 mm ID) was held along the central axis by an insulator mounted within a shielded cylinder. When an ion passes through the detector tube, an image charge of equal magnitude but opposite sign is induced. A lead connects the detector tube to a JFET which is in turn attached to a charge-sensitive pre-amplifier (Amptek A250). The A250 and JFET are housed in a grounded case mounted on the shield. The signal from the A250 is processed outside the vacuum chamber by a home-built analog to digital converter, which passes the signal into a computer where it is stored.

3. Energy selection

The energy distribution of the ions extracted from the hexapole was measured with a retarding potential energy analyzer. With a nominal ion energy of 100 eV, the baseline width of the energy distribution was around 10 eV. This width is mainly due to ions with energies lower than the nominal value and presumably results from collisions with the gas in the hexapole as the ions are being extracted. The dual HDA is employed to select a narrow band of energies for trapping in the cone trap. The HDA provides significant advantages over cylindrical analyzers in that it focuses ions in two directions and offers better energy resolution [31,32]. The resolution of the HDA is determined by three things: the size of the apertures, the maximum incident angular deviation ($\Delta\alpha$), and correction of the fringing fields. All three apertures (entrance, middle, and exit) are circular holes, 2.54 mm diameter. The entrance aperture size is the most easily controllable parameter for improving resolution as it also directly affects $\Delta\alpha$. The sizes for the middle and exit apertures were selected to match the size of the entrance aperture to ensure high energy resolution at the desired pass energy, $E_0 = V_0$. As the kinetic energy of an ion deviates from V_0, the trajectory it follows through the HDA diverges from R_0. A small aperture lowers the transmission efficiency but also guarantees that only a small window of kinetic energies is passed. The baseline energy resolution of a single HDA has been described by [33]

$$\frac{\Delta E}{E_0} = \frac{w}{2R_0} + \frac{1}{2}(\Delta\alpha)^2 \tag{3}$$

where w is the aperture diameter.

An einzel lens is located just before the entrance of the first HDA in order to control the entrance angle and the location of the focal point. Simion 7.0 simulations were used to optimize the performance of the lens and dual HDA. The best performance was obtained with the lens potentials set to cause the focal point of the ion beam to be within the HDA, instead of at the entrance aperture. The distribution of entrance angles through the HDA aperture was then ±0.0717 radians. Using this value for $\Delta\alpha$, the optimal resolution for the first HDA was calculated using Eq. (3) to be 5.3% (baseline) when the focal point was located within the HDA. If the focal point was located at the entrance aperture of the HDA, as is conventionally done, the acceptance angle increased to ±0.4643 radians (with a 2.54 mm diameter, 5.08 mm thick aperture) and the resolution was calculated to be 15.8% (baseline). Thus, a threefold improvement in resolution is achieved by simply adjusting the focal point of the einzel lens to fall within the HDA. The choice of focal point also helped to negate the fringing field effect, as discussed further below. According to the Simion simulations, the optimum resolution obtained for the einzel lens and dual HDA combination was 3.5% (baseline) with a pass energy spread of 98.5–102.0 eV.

The energy resolution can be improved by decelerating the ions prior to entry into the HDA, and then re-accelerating them to their original kinetic energy after they have been energy analyzed. Although the relative HDA resolution stays approximately the same when the ions are decelerated, the overall resolution improves because the energy analysis occurs at a lower kinetic energy. For example, deceleration to 10% of the initial kinetic energy, followed by energy selection in the HDA and re-acceleration, leads to around an order of magnitude improvement in the energy resolution. The base energy resolution improves to 0.45%, with an effective pass energy spread of 99.75–100.20 eV. This improvement in the resolution has a cost as it causes the transmitted signal to decrease by around an order of magnitude.

Incorporating the einzel lens before the first HDA improved the energy resolution in three ways: (1) it gave control over the entry angle ($\Delta\alpha$), (2) allowed the ions to be decelerated, and (3) helped with the fringing field correction. Fringing fields arise near the entrance and exit of an HDA. Ideally, all of the potential field lines in the HDA would be perfect hemispheres, concentric with R_0. However, the fields become distorted near the entrance and exit apertures where the hemispherical electrodes are in close proximity to the central grounded plate, which contains the entrance and exit apertures. Fringing field distortion causes the ions to not behave in an ideal fashion and can negatively affect the performance of the HDA. Numerous correction techniques have been formulated and tested to deal with this problem [30,34–39]. Many of these methods focus on improving the shape of the field lines to better approximate an ideal field. Most of the problems

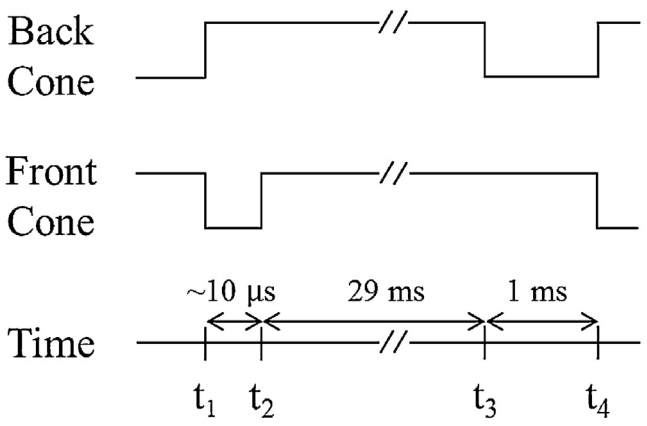

Fig. 3. Schematic diagram showing the pulse sequence used to trap an ion. A complete sequence is represented by times t_1 to t_4. At t_1 the trapping voltage (135 V) is applied to the back cone and the front cone is switched to zero volts to allow ions to enter the trap. Around 10 μs later (t_2) the voltage on the front cone is raised to 135 V to trap any ions in the trap. After 29 ms (t_3) the voltage on the back cone is lowered to evacuate the trap. After another 1 ms (t_4) the trap is reset and another trapping event begins.

associated with fringing fields and their correction techniques assume that the ion beam focal point is located at the entrance of the HDA, where the fields are at their least ideal. Another option is to focus the ions beyond the entrance aperture such that the focal point is located well past the fringing fields. We have combined this focusing technique with the fringing field corrector of Herzog [38,40], which involves spacing the HDA hemispheres a set distance (here, 3.175 mm) away from the central ground plate and apertures. This caused the fringing fields to follow a path which is more concentric with R_0 instead of converging at the point where the hemispheres are in close proximity to the central plate. The effects of the fringing fields were mitigated by this correction technique, though not completely negated.

Simion simulations have shown that having the focal point located inside the HDA leads to a distortion of the ion trajectory, with ions of a given energy tending not to follow the path of R_0. To account for this paracentric trajectory and ensure transmission of the desired kinetic energy, the middle aperture was placed 1.91 mm off of R_0. This in turn affected the focusing of the second HDA as the ions did not enter at R_0. Paracentric entry has been used by Zouros and co-workers [30,38,39,41] as a fringing field correction technique that improved the energy resolution, so this may also add to the resolution improvement here. Due to paracentric entry in the second HDA, ions with the desired kinetic energy did not exit at R_0. The final exit aperture was placed 3.05 mm off of R_0 to account for this.

4. Data collection and signal processing

As shown in Fig. 1, there are through holes in the end caps of the modified cone trap so that ions can enter and exit. The sequence of voltages placed on the end caps for trapping ions is shown in Fig. 3. The sequence begins at t_1 where the voltage on the back cone is raised to 135 V to reflect ions and the voltage on the front cone is dropped to zero volts so that ions can enter the trap. After around 10 μs (t_2) the voltage on the front cone is raised to 135 V to trap any ions that are in the trap. When the ion nears the end of the trap, the electric field generated by the end cap repels the ion and reverses its trajectory. This process is repeated as the ion passes through the trap in the opposite direction. As an ion passes back and forth through the charge detector tube, the image charge is recorded. After 29 ms (t_3) the voltage on the back cone is dropped to zero to empty the trap. After another 1 ms (t_4) the trap is reset and another trapping sequence begins. The number of ions that enter the trap is kept low enough that the probability of trapping more than one ion is small. In previous work, Benner [6] used the signal from the ion detector to trigger the closure of his trap. This approach leads to a high limit of detection (>250 e). Here we randomly close the trap, which allows us to look for much smaller signals but leads to a lower trapping efficiency (around 1%).

The periodic waveform which arises from the trapped ion is well suited to analysis with a fast Fourier transform. The resulting frequency domain spectrum contains the fundamental frequency of the oscillatory motion and the associated harmonics. The FFT magnitude is proportional to the image charge. The relationship between the m/z and the fundamental frequency, f, is given by:

$$\frac{m}{z} = \frac{C}{2E_0 f^2} \tag{4}$$

where C is a constant that depends on the geometry of the cone trap and the applied voltages. The kinetic energy (E_0) is selected by the dual HDA.

Simion simulations of the ion trap were performed in order to determine the constant C and hence calibrate the relationship between the fundamental frequency and the m/z at a given kinetic energy. First, the minimum and maximum incident angles were determined trigonometrically from different radial starting positions, and then a series of possible ion trajectory paths were generated. Simion updates the ion trajectory using a Runge–Kutta method, performed at discrete time steps which are not always uniformly spaced. In order to better approximate the true ion signal, a user program was written which set the time step to be either 1% or 0.1% of the actual sampling period of the data acquisition boards (~533 ns). This allowed better resolution of the ion's trajectory and improved sampling for analyzing the simulated signal. However, there were periods in the ion flight path when the time steps suggested by the Runge–Kutta routine in Simion were smaller than defined within the user program. In these cases, the Runge–Kutta time step was used. After such an event, the next time step was adjusted so that the total time was once again a multiple of the user defined time step. The total time-of-flight and xyz position were recorded at each multiple of the user defined time step.

This simulated signal was transferred to a waveform generator for use in calibration of the charge detector. Calibration was performed by applying a voltage across a known capacitance into the gate of the JFET. This was done with several different voltages and frequencies. The resulting signal was analyzed with a Fortran program to yield the charge calibration.

5. Determination of the charge measurement error

Simulations were performed in order to determine the charge measurement error and the limit of detection expected from the experiments. Noise files were recorded by applying all the voltages to the experiment, except that no ions were introduced into the vacuum chamber. Simulated ion signals for charge states from 20 to 100 electrons were added to the noise files and the resulting signals were analyzed by the program used to analyze the real data. Each simulated ion was given a random oscillation frequency, trapping time, and starting time. The frequencies were limited to those corresponding to m/z values between 500 and 3000, the minimum trapping time was set to be equivalent to 400 cycles, and the maximum trapping time was 30 ms. For ions with charges of 30 e and greater, all of the simulated signals were found by the data analysis program. However, for charges less than 30 e, some of the simulated signals were not picked up. For a charge of 20 e, only 16 out of 42 simulated signals were found. The upper half of Fig. 4 shows the average charge found by the data analysis program plotted against the input charge. The plot is linear down to around below 30 e,

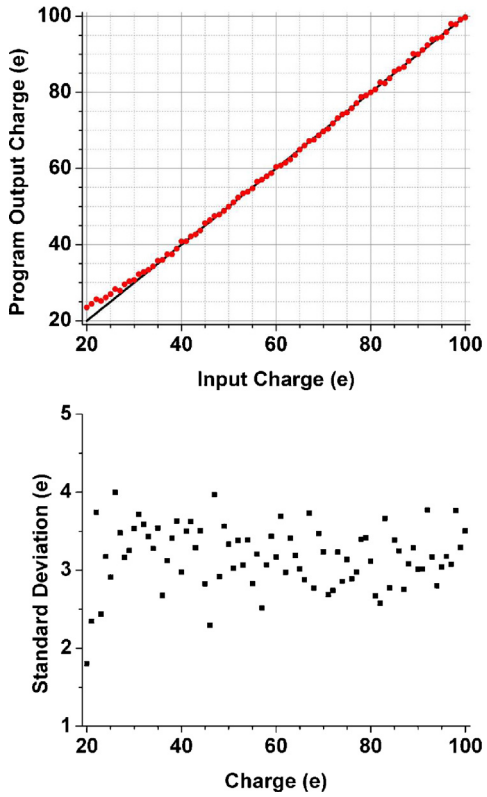

Fig. 4. The top panel shows the output response (red circles) of the data analysis program as a function of known input charge. The black line represents the ideal response. The bottom panel shows the standard deviation of the response as a function of charge. (For interpretation of the references to color in this figure legend, the reader is referred to the web version of the article.)

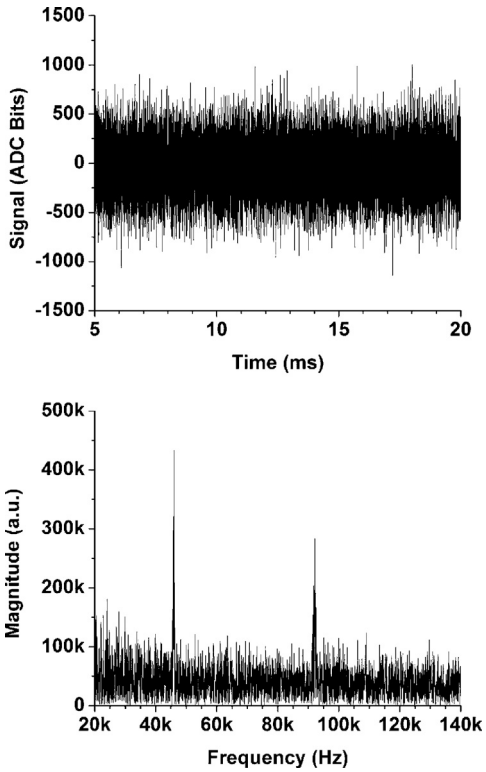

Fig. 5. The top panel shows a portion of a raw signal containing a BSA +56 ion which was trapped for 25 ms (1135 cycles). The signal shown here was passed through a 10 kHz FFT high pass filter. The bottom panel shows the Fourier transform of the signal from the top panel. The ion has a fundamental frequency of ~46 kHz, corresponding to an m/z of ~1200 Da/e. The first harmonic can also be seen at ~92 kHz.

where the program begins to lose some of the signals. The deviations below 30 e may result from selective detection of signals that are reinforced by the noise. The lower half of Fig. 4 shows the standard deviation plotted against input charge. The standard deviation is independent of input charge, and has an average value of 3.2 e. This represents the measurement error expected for the charge. Based on these results, we can expect to detect nearly all ions with charges of 30 e and above with an average measurement error of 3.2 e.

6. Experimental results

The upper half of Fig. 5 shows an example of a raw time domain signal for a trapped ion. The Fourier transform of this signal is shown in the lower half of Fig. 5. The peak at around 46 kHz is the fundamental frequency, which corresponds to an m/z of ~1200 Da/e. The first harmonic can be seen at around 92 kHz. The magnitude of the fundamental indicates that the ion has a charge of 56 e.

Results from an experiment where 3300 BSA ions were trapped sequentially and their signals recorded are shown in Fig. 6. In this data set the ions were trapped for an average of 325 cycles. The maximum number of cycles was 1139, corresponding to a trapping time of ~25 ms. The upper plot in Fig. 6 shows the m/z distribution determined from the measured oscillation frequencies. The distribution peaks at around 1250 Da/e. The middle plot in Fig. 6 shows the measured charge distribution. Ions with a charge as low as 17 e were detected, but any ion with a charge less than 30 e was discarded because the uncertainty in the charge begins to diverge for charges smaller than 30 e. The charge distribution is bimodal. The major peak occurs at around 50 e, and there is a minor peak at around 100 e. The mass distribution is shown in the lower plot in Fig. 6. The mass distribution is also bimodal with the major peak at around 65 kDa and the minor peak at around 130 kDa. We attribute these peaks to the monomer and dimer of BSA. The nominal mass of BSA is 66.4 kDa, so both peaks occur at a mass that is slightly lower than expected. The discrepancy between the measured masses and the expected values probably results from a small error in the charge calibration. Although not visible on these plots, it is worth noting that a number of ions were detected with masses corresponding to the trimer of BSA. In other experiments we have observed ions with masses corresponding to the tetramer and pentamer of BSA.

We performed simulations of the BSA m/z, charge, and mass distributions to compare with the measured data. The simulations were performed using the scheme outlined above where artificial signals are added to noise files, and then analyzed. Simulations were performed for around 1500 BSA ions and twice the number of dimer ions (since more charge states are available for the dimer). For the BSA monomer we used ions with 28–52 charges, and for the BSA dimer we used ions with 56–104 charges. To facilitate comparison with the measured spectra, after the simulations were performed the relative abundances of the monomer and dimer ions were adjusted so that they roughly match the experimental values. The results are shown in Fig. 7.

The upper plot in Fig. 7 shows the m/z distribution. The bin width used here is narrow enough to reveal the charge state distribution. The FFT determines the oscillation frequency of the simulated signals with sufficient accuracy to resolve the charge states. The frequency determined from the FFT analysis deviates from the input value by less than 0.1%. The charge distribution obtained from this analysis of the simulated signals is shown in the middle plot of Fig. 7. The individual charge states are not resolved here

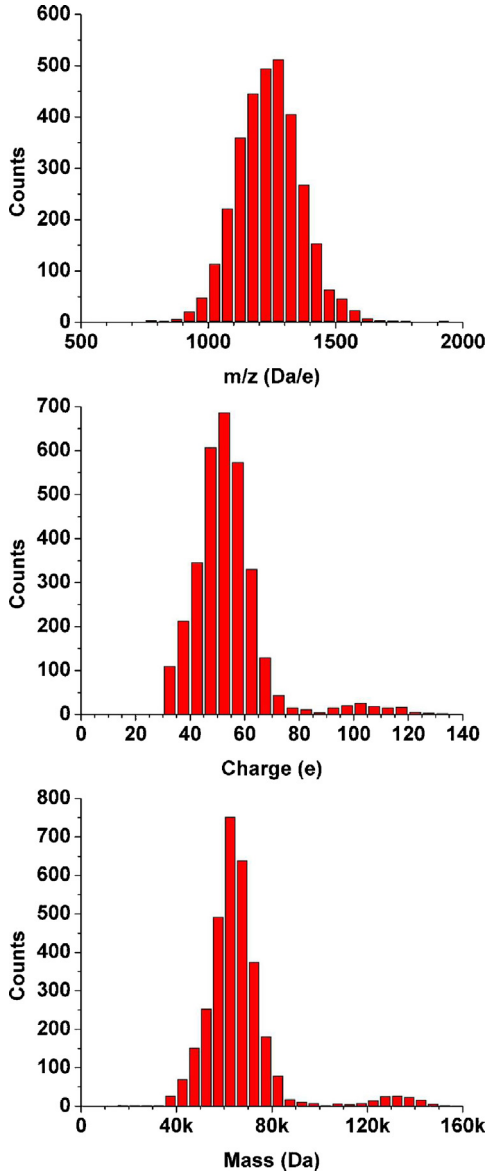

Fig. 6. Experimental results for BSA. The top panel shows the m/z distribution, the middle panel shows the charge state distribution, and the bottom panel shows the mass distribution.

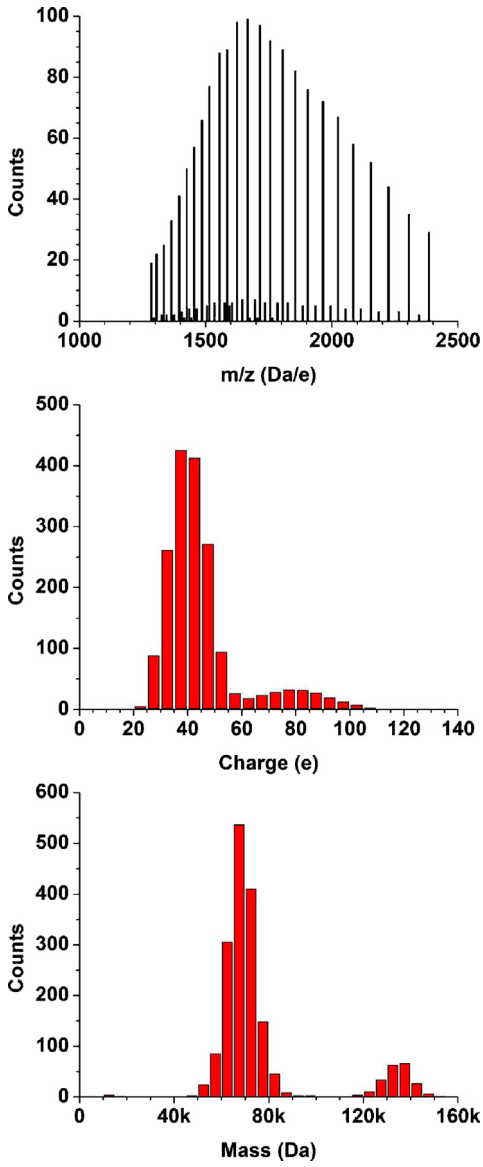

Fig. 7. Simulation results for BSA. The top panel shows the m/z distribution obtained by analyzing simulated BSA signals (see text) with the data analysis program. The middle panel shows the charge distribution, and the bottom panel shows the mass distribution.

because the charge is only determined with an accuracy of 3.2 e. The charge distribution is bimodal, reflecting the different charges on the monomer and dimer. The simulated mass distribution is shown in the lower plot in Fig. 7. There are two peaks corresponding to the masses of the monomer and dimer.

7. Discussion

The monomer peak in the simulated mass distribution (lower plot in Fig. 7) is around 13.2 kDa wide at the half height. This width results almost entirely from the uncertainty in the charge determination (3.2 e). The peak in the measured mass distribution is slightly broader, around 17.0 kDa wide at half height. A large fraction of the difference between widths of the measured and simulated distributions can be attributed to the finite energy spread of the ions entering the trap. In the simulations it is assumed that the width of the energy distribution is vanishingly small while the measurements shown in Fig. 6 were performed under medium resolution condition with a nominal energy spread of 3.5 eV. Under high energy resolution conditions (i.e., with the ions decelerated before transmission through the energy analyzer) the width of the mass distribution narrows to around 14.0 kDa at the half height. With the high energy resolution, the measured width of the mass distribution should correspond closely to the simulated width. The fact that there is still a small discrepancy (14.0 kDa versus 13.2 kDa) suggests that another factor contributes a small amount to the width.

In the simulations it is assumed that the ions' masses correspond exactly to the mass of the BSA monomer or dimer ions. Any broadening of the m/z peaks in the experiments due to counter ions or adduct formation will contribute to the width of the mass distribution. In the m/z distribution measured with the time-of-flight mass spectrometer the peaks are not baseline resolved indicating that the finite width of the m/z peaks could be a factor, and contribute a small amount to the width of the mass distribution.

The fact that the measured mass distribution is only slightly broader than the simulated one confirms the reliability of the

average uncertainty in the charge determination obtained from the simulations (3.2 e).

8. Conclusions

We have described a new charge detection mass spectrometer employing an ion trap to recirculate the ions. The main innovations described here are: (1) use of a dual hemispherical deflection analyzer to preselect the ion energy before the ions enter the trap; (2) use of modified cone trap to provide more oscillations; and (3) use of an FFT to analyze the results. With these innovations we have reduced the limit of detection to 30 e, which is a significant improvement over the previous best of 100 e achieved with a detector array [11]. The charge is measured with an average accuracy of 3.2 e.

The mass resolution achieved here with BSA (14 kDa) is mainly limited by the uncertainty in the charge measurement. Further improvements in charge detection mass spectrometry will hinge on further improving the accuracy of the charge determination.

Acknowledgements

We gratefully acknowledge the support of the National Science Foundation through award number 0832651. This work was partially supported by a grant from the METACyt Initiative, Indiana University. We are grateful for the technical assistance of Mr. John Poehlman and Mr. Andy Alexander in Electronic Instrument Services and Mr. Delbert Allgood in Mechanical Instrument Services. We thank Staci Anthony for performing some of the Simion simulations on the ion trap.

References

[1] H. Shelton, C.D. Hendricks, R.F. Wuerker, Electrostatic acceleration of microparticles to hypervelocities, Journal of Applied Physics 31 (1960) 1243–1246.
[2] J.F. Friichtenicht, Micrometeroid simulation using nuclear accelerator techniques, Nuclear Instruments and Methods 28 (1964) 70–78.
[3] C.D. Hendricks, Charged droplet experiments, Journal of Colloid Science 17 (1962) 249–259.
[4] S.D. Fuerstenau, W.H. Benner, Molecular weight determination of megadalton DNA electrospray ions using charge detection time-of-flight mass spectrometry, Rapid Communications in Mass Spectrometry 9 (1995) 1528–1538.
[5] J.C. Schultz, C.A. Hack, W.H. Benner, Mass determination of megadalton-DNA electrospray ions using charge detection mass spectrometry, Journal of the American Society for Mass Spectrometry 9 (1998) 305–313.
[6] W.H. Benner, Gated electrostatic ion trap to repetitiously measure the charge and *m/z* of large electrospray ions, Analytical Chemistry 69 (1997) 4162–4168.
[7] S.D. Fuerstenau, W.H. Benner, J.J. Thomas, C. Brugidou, B. Bothner, G. Siuzdak, Mass spectrometry of an intact virus, Angewandte Chemie International Edition 40 (2001) 541–544.
[8] S.D. Fuerstenau, Whole virus mass analysis by electrospray ionization, Journal of the Mass Spectrometry Society of Japan 51 (2003) 50–53.
[9] M. Gamero-Castaño, Induction charge detector with multiple sensing stages, Review of Scientific Instruments 78 (2007) 043902.
[10] M. Gamero-Castaño, Retarding potential and induction charge detectors in tandem for measuring the charge and mass of nanodroplets, Review of Scientific Instruments 80 (2009) 053301.
[11] J.W. Smith, E.E. Siegel, J.T. Maze, M.F. Jarrold, Image charge detection mass spectrometry: pushing the envelope with sensitivity and accuracy, Analytical Chemistry 83 (2011) 950–956.
[12] J.T. Maze, T.C. Jones, M.F. Jarrold, Negative droplets from positive electrospray, Journal of Physical Chemistry A 110 (2006) 12607–12612.
[13] L.W. Zilch, J.T. Maze, J.W. Smith, G.E. Ewing, M.F. Jarrold, Charge separation in the aerodynamic breakup of micrometer-sized water droplets, Journal of Physical Chemistry A 112 (2008) 13352–13363.
[14] L.W. Zilch, J.T. Maze, J.W. Smith, M.F. Jarrold, Freezing, fragmentation, and charge separation in sonic sprayed water droplets, International Journal of Mass Spectrometry 283 (2009) 191–199.
[15] T. Doussineau, M. Kerleroux, X. Dagany, C. Clavier, M. Barbaire, J. Maurelli, R. Antoine, Ph. Dugourd, Charging megadalton poly(ethylene oxide)s by electrospray ionization: a charge detection mass spectrometry study, Rapid Communications in Mass Spectrometry 25 (2011) 617–623.
[16] T. Doussineau, C.Y. Bao, C. Clavier, X. Dagany, M. Kerleroux, R. Antoine, Ph. Dugourd, Infrared multiphoton dissociation tandem charge detection-mass spectrometry of single megadalton electrosprayed ions, Review of Scientific Instruments 82 (2011) 084104.
[17] M. Dahan, R. Fishman, O. Heber, M. Rappaport, N. Altstein, D. Zajfman, W.J. van der Zande, A new type of electrostatic ion trap for storage of fast ion beams, Review of Scientific Instruments 69 (1998) 76–83.
[18] H.B. Pedersen, D. Strasser, S. Ring, O. Heber, M.L. Rappaport, Y. Rudich, I. Sagi, D. Zajfman, Ion motion synchronization in an ion-trap resonator, Physical Review Letters 87 (2001) 055001.
[19] D. Zajfman, O. Heber, M.L. Rappaport, H.B. Pedersen, D. Strasser, S. Goldberg, Self-bunching effect in an ion trap resonator, Journal of the Optical Society of America B 20 (2003) 1028–1032.
[20] S. Ring, H.B. Pedersen, O. Heber, M.L. Rappaport, P.D. Witte, K.G. Bhushan, N. Altstein, Y. Rudich, I. Sagi, D. Zajfman, Fourier transform time-of-flight mass spectrometry in an electrostatic ion beam trap, Analytical Chemistry 72 (2000) 4041–4046.
[21] D. Zajfman, Y. Rudich, I. Sagi, D. Strasser, D.W. Savin, S. Goldberg, M. Rappaport, O. Heber, High resolution mass spectrometry using a linear electrostatic ion beam trap, International Journal of Mass Spectrometry 229 (2003) 55–60.
[22] H.T. Schmidt, H. Cederquist, J. Jensen, A. Fardi, Conetrap: a compact electrostatic ion trap, Nuclear Instruments and Methods in Physics Research Section B 173 (2001) 523–527.
[23] D. Roy, D. Tremblay, Design of electron spectrometers, Reports on Progress in Physics 53 (1990) 1621–1674.
[24] J.H. Vilppola, J.T. Keisala, P.J. Tanskanen, Optimization of hemispherical electrostatic analyzer manufacturing with respect to resolution requirements, Review of Scientific Instruments 64 (1993) 2190–2194.
[25] R.T. Kelly, A.V. Tolmachev, J.S. Page, K. Tang, R.D. Smith, The ion funnel: theory, implementation, and applications, Mass Spectrometry Reviews 29 (2010) 294–312.
[26] K. Kurihara, Low-aberration einzel lens for a focused-ion-beam system, Japan, Journal of Applied Physics: Part 1 24 (1985) 225–230.
[27] K. Saito, T. Okubo, K. Takamoto, Design method for an electrostatic einzel lens having an asymmetric structure, Journal of Vacuum Science and Technology A 4 (1986) 226–229.
[28] R.A. Colman, G.J.F. Legge, Measurement of the optical properties of an asymmetric einzel lens using the two-grid method, Journal of Applied Physics 74 (1993) 1484–1491.
[29] B.A. Mamyrin, Time-of-flight mass spectrometry (concepts, achievements, and prospects), International Journal of Mass Spectrometry 206 (2000) 251–266.
[30] E.P. Benis, T.J.M. Zouros, Improving the energy resolution of a hemispherical spectrograph using a paracentric entry at a non-zero potential, Nuclear Instruments and Methods in Physics Research Section A 440 (2000) 462–465.
[31] E.M. Purcell, The focusing of charged particles by a spherical condenser, Physical Review 54 (1938) 818–826.
[32] C.E. Kuyatt, J.A. Simpson, Electron monochromator design, Review of Scientific Instruments 38 (1967) 103–111.
[33] J.H. Moore, C.C. Davis, M.A. Coplan, Building Scientific Apparatus: A Practical Guide to Design and Construction, Perseus Books, Cambridge, MA, 2003.
[34] H. Wollnik, H. Ewald, The influence of magnetic and electric fringing fields on the trajectories of charged particles, Nuclear Instruments and Methods 36 (1965) 93–104.
[35] K. Jost, Fringing field correction for 127° and 180° electron spectrometers, Journal of Physics E 12 (1979) 1001–1005.
[36] S.G. Anderson, K.W. Sohlberg, S.L. Howard, A.K. Shukla, J.H. Futrell, A high transmission hemispherical energy analyzer for ion spectrometry, Journal of the American Society for Mass Spectrometry 2 (1991) 506–510.
[37] A. Baraldi, V.R. Dhanak, G.C. King, A fringing field corrector for the boundary between two electrostatic deflection analysers placed in tandem, Measurement Science and Technology 3 (1992) 778–779.
[38] O. Sise, T.J.M. Zouros, M. Ulu, M. Dogan, Comparison of fringing field correction schemes for the 180° hemispherical deflector analyzer, Physics Procedia 1 (2008) 473–477.
[39] O. Sise, M. Ulu, M. Dogan, G. Martinez, T.J.M. Zouros, Fringing field optimization of hemispherical deflector analyzers using BEM and FDM, Journal of Electron Spectroscopy and Related Phenomena 177 (2010) 42–51.
[40] R. Herzog, Ablenkung von Kathoden- und Kanalstrahlen am Rande eines Kondensators, dessen Streufeld durch eine Blende begrenzt Ist, Zeitschrift für Physik A Hadrons and Nuclei 97 (1935) 596–602.
[41] T.J.M. Zouros, E.P. Benis, The hemispherical deflector analyser revisited. I. Motion in the ideal 1/r potential, generalized entry conditions, kepler orbits and spectrometer basic equation, Journal of Electron Spectroscopy and Related Phenomena 125 (2002) 221–248.